Two-dimensional effects on electrostatic instabilities in Hall thrusters. II. Comparison of particle-in-cell simulation results with linear theory dispersion relations

Federico Petronio, Thomas Charoy, Alejandro Alvarez Laguna, Anne Bourdon, Pascal Chabert

Two-dimensional effects on electrostatic instabilities in Hall Thrusters. II. Comparison of particle-in-cell simulation results with linear theory dispersion relations.

Federico Petronio,[1,2] Thomas Charoy,[1] Alejandro Alvarez Laguna,[1] Anne Bourdon,[1] and Pascal Chabert[1]

[1)]*Laboratoire de Physique des Plasmas (LPP), CNRS, Sorbonne Université, École Polytechnique, Institut Polytechnique de Paris, 91120 Palaiseau, France.*

[2)]*Safran Aircraft Engines, Electric Propulsion Unit, 27208 Vernon, France.*

(*Electronic mail: federico.petronio@lpp.polytechnique.fr)

(Dated: 2 December 2022)

Two-dimensional effects on electrostatic instabilities II

In Paper I we successfully used an external circuit to significantly damp the Breathing Mode (BM) oscillations in 2D Particle-in-Cell (PIC) self-consistent simulations of the axial-azimuthal plane of an Hall thruster (HT). We also introduced the two-point power spectral density reconstruction method (PSD2P) used to analyze electrostatic instabilities and generate dispersion diagrams in azimuthal and axial directions, at various times during the BM period. Here, a 3D Dispersion Relation (DR) for electrostatic modes is calculated by linearizing the continuity/momentum fluid equations for electrons and ions. We show that by taking the appropriate limits, this relation can be simplified to derive the DRs of some well-known $\mathbf{E} \times \mathbf{B}$ instabilities, such as the Electron Cyclotron Drift Instability (ECDI), and its evolution to the Ion Acoustic Wave (IAW), and the Ion Transit-Time Instability (ITTI). The PSD2P diagrams demonstrate the importance of considering the 2D nature of the IAW and ITTI, that have been previously considered mono-dimensional (azimuthal and axial, respectively). In particular, we show that the IAW grows near the maximum of the magnetic field, and due to its axial components propagates towards both the anode and the cathode (in addition to the well-known azimuthal propagation). The resulting wavefront is therefore bent. By analogy to the propagation of acoustic waves in gases, it is proposed that the cause of the IAW wavefront bending is the strong electron temperature gradients in the axial direction. We also show that the ITTI has a strong positive growth rate when a small azimuthal component is present. Finally, we observe that the ITTI significantly affects the discharge current.

I. INTRODUCTION

Hall Thrusters (HTs) are flight-proven space propulsion systems, however their development is semi-empirical because the fundamental physics governing these devices is still poorly understood[1,2]. In recent years, the market for satellites[3] has required the development of new propulsion systems with a reduced thrust and power consumption[4], and it showed that the development of new prototypes of HTs remains a long and costly trial-and-error route. Different models and simulations of HTs have been developed over the years (see, e.g., Hara[5] or Taccogna et al.[6] for a recent review of models) to study the complex discharge physics in HTs and understand which parameters impact the most the thruster performances. The challenge in coming years is to derive predictive models to help designing new thrusters and reduce the cost and duration of experimental tests[7,8].

Current computational models can be classified into three main categories that we list below in ascending order of computational cost: (i) fluid simulations[9–11], where all species are considered with a fluid approach, (ii) hybrid simulations[12–14], where the electrons are treated as a fluid while ions and/or neutrals are treated as discrete particles and (iii) Particle-in-Cell (PIC) simulations[15–17] where a kinetic description of all the charged species is adopted. The first works focused on the axial direction[18], i.e., the direction of the thrust, given its relevance for industrial applications. Later works focused on the radial and radial-axial directions[19,20] to study the effect of the plasma sheaths and plasma wall interaction. The novelty of the last two decades is the rising interest in the dynamics occurring in the azimuthal direction[21–26], i.e., the direction that is perpendicular to both the electric and magnetic fields. The waves propagating in this direction have been found to impact the mobility of electrons along the axial direction of the thruster, which has a fundamental impact on the performance and behavior of HTs.

HTs have a large number of plasma instabilities from kHz to tens of MHz, that propagate both in the azimuthal and axial directions. These instabilities have been extensively studied theoretically[1,23,24,27–32], numerically[5,7,33] and experimentally[12,34,35]. However, due to their complexity and the interplay between these instabilities, the underlying physics is still not fully understood. The Electron Cyclotron Drift Instability (ECDI) is a short-wavelength ($\lambda \sim 1\,\mathrm{mm}$) high-frequency ($\omega \sim 7\,\mathrm{MHz}$) electrostatic instability that develops mainly along the $\mathbf{E} \times \mathbf{B}$ drift direction. This instability has been studied during the last 20 years[6,15,21,22,24,32,36–38] and has shown to have a significant impact on the electron transport in axial direction. PIC simulations[16,25,39]

have revealed that this instability evolves towards the Ion Acoustic Wave (IAW) after some tens of microseconds. For this reason, in the following, we will refer to the ECDI/IAW instability. In addition to the ECDI, numerical studies have shown a radial-azimuthal electrostatic instability that was named the Modified Two-Stream Instability (MTSI) with a longer wavelength (some millimeters) and a frequency in the MHz range[17,37,39,40]. Hagelaar *et al.*[41], Barral *et al.*[42] and Fernandez *et al.*[43] introduced an axial electrostatic long-wavelength ($\sim 1\,$cm) mid-frequency ($\sim 400\,$kHz) instability that was called Ion Transit-Time Instability (ITTI). This instability develops in the thruster plume and its period is of the order of the duration of the transit of ions in the acceleration region. This instability is a resistive instability, whose azimuthal propagation was studied by Litvak and Fisch[44]. Koshkarov *et al.*[45] have studied the axial growth and propagation of this mode. Recently, Charoy *et al.*[46] have shown the influence of the ITTI on the ion ejection velocity in PIC simulations. In the same frequency range, some experimental and numerical studies[47,48] have observed the Ion-Ion Two Stream Instability (IITSI), which is related to the presence of doubly charged ions. Finally, in the low-frequency range ($\sim 10\,$kHz), the Breathing Mode (BM) is found as a low-frequency ionization instability. Despite the origin of this instability not being fully understood[49,50], it is commonly accepted that the BM should not be considered among electrostatic plasma instabilities.

Ducrocq *et al.*[31] derived the three-dimensional kinetic dispersion relation to study electrostatic instabilities in $\mathbf{E}\times\mathbf{B}$ plasmas in conditions similar to those in HTs. Cavalier *et al.*[32] solved numerically and analyzed this DR in some relevant planes of the HTs. In the present work, we calculate the 3D fluid electrostatic dispersion relation (DR) for a plasma in an $\mathbf{E}\times\mathbf{B}$ configuration using the linear perturbation method. We will show that IAW, MTSI and ITTI can be found from this dispersion relation. The ECDI is a purely kinetic instability, that consequently cannot be retrieved from fluid theory. Nevertheless, a comparison between the kinetic DR and the fluid one is proposed to understand the connection between this instability and the IAW. In this work, we will focus on the electrostatic instabilities of a singly-ionized plasma. For this reason, we will not study the BM and IITSI, even though the BM is present in our simulations.

In Paper I, we presented 2D PIC simulations of the axial-azimuthal plane of a Hall Thruster coupled to a fluid model for the gas. These simulations were able to capture the BM with realistic current oscillations, thanks to the introduction of a circuit that models the RLC filter used in real devices. We verified that the use of the permittivity scaling technique (that is employed to speed up the simulations for several BM cycles) allows for the growth of the axial-azimuthal plasma

instabilities. In addition, we discussed the implications of this technique on the discharge characteristics. Finally, we presented the two-point power spectral density (PSD2P) method that allows for a local reconstruction of the instability spectrum along the axis. We applied this method to two $4\,\mathrm{cm} \times 4\,\mathrm{cm}$ PIC simulations with different cathode injection temperatures (i.e. T_e^{cath} fixed to 0.1 or 5 eV). For both injection temperatures, we observed that the ECDI/IAW instability dominates during the growing phase of the BM, while the ITTI is predominant in the decreasing phase of the BM. However, the injection temperature has shown to play a role in the development of the instabilities. In the case with low temperature, i.e., $T_e^{cath} = 0.1\,\mathrm{eV}$ (named "case B" in Paper I), the ITTI is not present during the growing phase of the current whereas the IAW/ECDI disappears during the decreasing phase. In the case with $T_e^{cath} = 5\,\mathrm{eV}$ (named "case A" in Paper I) we observed a persistent ITTI during both phases of the BM.

In the present work, we focus on the case with the low injection temperature, i.e. $T_e^{cath} = 0.1\,\mathrm{eV}$, as it gives the possibility to study the two instabilities separately. The different phases of this simulation are analyzed in detail in Section III, where we compare the PSD2P maps to the analytical DRs obtained in Section II. The analysis reveals key observations about the nature and the development of these $\mathbf{E} \times \mathbf{B}$ instabilities.

II. 3D FLUID ELECTROSTATIC DISPERSION RELATION

In this section, we derive the DR from a fluid model that considers the continuity and momentum equations for electrons and ions, coupled by the Poisson equation. The derivation in this Section does not introduce any new instability: we derive a general 3D DR and we show precisely the intervals of validity of the most studied DRs in HTs. Moreover, with a top-down approach we show that it is possible to calculate a 2D version of the DRs of some instabilities that are usually considered as mono-dimensional. We refer to the azimuthal direction as y, the axial direction as x and the radial direction as z. We consider the magnetic field $\mathbf{B} = B\hat{\mathbf{e}}_z$ is along the z direction, the stationary electric field $\mathbf{E} = E\hat{\mathbf{e}}_x$ is along the x direction and the $\mathbf{E} \times \mathbf{B}$ drift occurs in the negative y direction.

Ions and electrons are assumed to be isothermal with an isotropic temperature. In typical HTs the electrons are magnetized while ions are not. Consequently, we neglect the effect of the magnetic field on ions. We perform a first-order perturbation of the densities, the velocities and of the potential and all the variables are written in the form $\Gamma = \Gamma_0 + \Gamma'$, where Γ_0 is the equilibrium

and Γ' a small perturbation. The linearized fluid equations read

$$\begin{aligned}
&\frac{\partial n_e'}{\partial t} + \mathbf{v}_{e0}\cdot\nabla n_e' + n_0\nabla\cdot\mathbf{v}_e' = 0,\\
&\frac{\partial n_i'}{\partial t} + \mathbf{v}_{i0}\cdot\nabla n_i' + n_0\nabla\cdot\mathbf{v}_i' = 0,\\
&\frac{\partial \mathbf{v}_e'}{\partial t} + \mathbf{v}_{e0}\nabla\cdot\mathbf{v}_e' = -\frac{e}{m_e}(\mathbf{E}' + \mathbf{v}_e'\times\mathbf{B}) - \frac{k_b T_e}{m_e n_{e0}}\nabla n_e' - \nu_e\mathbf{v}_e',\\
&\frac{\partial \mathbf{v}_i'}{\partial t} + \mathbf{v}_{i0}\nabla\cdot\mathbf{v}_i' = \frac{e\mathbf{E}'}{m_i} - \frac{k_b T_i}{m_i n_{i0}}\nabla n_i' - \nu_i\mathbf{v}_i',
\end{aligned}$$

and the Poisson equation reads

$$\nabla^2\Phi' = \frac{-e}{\varepsilon_0}(n_i' - n_e'). \tag{1}$$

Here, $n_{i,e}$ are the ion and electron densities, $\mathbf{v}_{i,e}$ are the ion and electron velocities, $\nu_{i,e}$ are the ion and electron collision frequencies, $m_{i,e}$ are the ion and electron masses, $T_{i,e}$ are the ion and electron temperatures, $\mathbf{E}$ is the electric field, $\mathbf{B}$ is the magnetic field, k_b is the Boltzmann constant and e is the elementary charge. The ionization has been neglected in the system.

Let us now consider a planar wave perturbation, i.e. $\Gamma' = \tilde{\Gamma}\exp[\imath(\mathbf{k}\cdot\mathbf{x} - \omega t)]$. By defining $\bar{\omega}_{e,i} \doteq \omega - \mathbf{k}\cdot\mathbf{v}_{e,i,0}$, the continuity equations can be written as

$$\frac{\tilde{n}_e}{n_0} = \frac{\mathbf{k}\cdot\tilde{\mathbf{v}}_e}{\bar{\omega}_e}, \tag{2}$$

$$\frac{\tilde{n}_i}{n_0} = \frac{\mathbf{k}\cdot\tilde{\mathbf{v}}_i}{\bar{\omega}_i}, \tag{3}$$

for electrons and ions, respectively. The discussion on the momentum equations has to be held separately for ions and electrons, since the former are not magnetized, while the latter are. With $\hat{\omega}_{e,i} \doteq \omega - \mathbf{k}\cdot\mathbf{v}_{e,i,0} + \imath\nu_{e,i}$, the linearized momentum equation for non-magnetized isothermal ions reads

$$\tilde{\mathbf{v}}_i = \frac{\left(v_{th,i}^2\frac{\tilde{n}_i}{n_0} - \frac{e\tilde{\Phi}}{m_i}\right)\mathbf{k}}{\hat{\omega}_i}, \tag{4}$$

where $v_{th,i} = (k_b T_i/m_i)^{1/2}$ is the ion thermal velocity. The electron momentum equation is more complex, since the equations in x and y directions are coupled by the magnetic field. The linearized vector equation for isothermal magnetized electrons is

$$-\imath\omega m_e\tilde{\mathbf{v}}_e + m_e\tilde{\mathbf{v}}_e(\imath\mathbf{k}\cdot\mathbf{v}_{e0}) = e\tilde{\Phi}\imath\mathbf{k} - \tilde{\mathbf{v}}_e\times\mathbf{B} - m_e v_{th,e}^2\imath\mathbf{k} - m_e\nu_e\tilde{\mathbf{v}}_e.$$

Each component reads

$$\begin{aligned}
\tilde{v}_{ex}\left(\omega-\mathbf{k}\cdot\mathbf{v}_{e0}+\imath\nu_e\right) &= \left(v_{th,e}^2\frac{\tilde{n}_e}{n_0}-\frac{e\tilde{\Phi}}{m_e}\right)k_x-\imath\tilde{v}_{ey}\omega_{ce},\\
\tilde{v}_{ey}\left(\omega-\mathbf{k}\cdot\mathbf{v}_{e0}+\imath\nu_e\right) &= \left(v_{th,e}^2\frac{\tilde{n}_e}{n_0}-\frac{e\tilde{\Phi}}{m_e}\right)k_y+\imath\tilde{v}_{ex}\omega_{ce},\\
\tilde{v}_{ez}\left(\omega-\mathbf{k}\cdot\mathbf{v}_{e0}+\imath\nu_e\right) &= \left(v_{th,e}^2\frac{\tilde{n}_e}{n_0}-\frac{e\tilde{\Phi}}{m_e}\right)k_z.
\end{aligned}$$

In the previous equations we introduced the electron thermal velocity $v_{th,e}=(k_bT_e/m_e)^{1/2}$ and the cyclotron frequency $\omega_{ce}=qB/m_e$. We solve the above system for the three velocity components, as follows

$$\begin{aligned}
\tilde{v}_{ex} &= \left(v_{th,e}^2\frac{\tilde{n}_e}{n_0}-\frac{e\tilde{\Phi}}{m_e}\right)\frac{(\hat{\omega}_e k_x-\imath\omega_{ce}k_y)}{\hat{\omega}_e^2-\omega_{ce}^2},\\
\tilde{v}_{ey} &= \left(v_{th,e}^2\frac{\tilde{n}_e}{n_0}-\frac{e\tilde{\Phi}}{m_e}\right)\frac{(\hat{\omega}_e k_y+\imath\omega_{ce}k_x)}{\hat{\omega}_e^2-\omega_{ce}^2},\\
\tilde{v}_{ez} &= \left(v_{th,e}^2\frac{\tilde{n}_e}{n_0}-\frac{e\tilde{\Phi}}{m_e}\right)\frac{k_z}{\hat{\omega}_e}.
\end{aligned}\tag{5}$$

Note that x and y are coupled, while the z direction (parallel to $\mathbf{B}$) is independent, as expected. By combining Eq. (4) and Eq. (5) with Eq. (3) and Eq. (2), respectively, we obtain

$$\begin{aligned}
\frac{\tilde{n}_i}{n_0} &= \frac{\frac{e\tilde{\Phi}}{m_i}k^2}{\hat{\omega}_i\bar{\omega}_i-k^2v_{th,i}^2},\\
\frac{\tilde{n}_e}{n_0} &= \frac{-\frac{e\tilde{\Phi}}{m_e}\left(\hat{\omega}_e^2k^2-\omega_{ce}^2k_z^2\right)}{\hat{\omega}_e(\hat{\omega}_e^2-\omega_{ce}^2)\bar{\omega}_e-\hat{\omega}_e^2k^2v_{th,e}^2+\omega_{ce}^2k_z^2v_{th,e}^2}.
\end{aligned}$$

These expressions can be injected in the linearized Poisson equation, that reads

$$k^2\tilde{\Phi}=\frac{en_0}{\varepsilon_0}\left(\frac{\tilde{n}_i}{n_0}-\frac{\tilde{n}_e}{n_0}\right),$$

to obtain the following isothermal fluid dispersion relation for a partially magnetized plasma :

$$0=1+\chi_i+\chi_e=1-\frac{\omega_{pi}^2}{\hat{\omega}_i\bar{\omega}_i-k^2v_{th,i}^2}-\frac{\omega_{pe}^2\left(\hat{\omega}_e^2-\frac{k_z^2}{k^2}\omega_{ce}^2\right)}{\hat{\omega}_e\left(\hat{\omega}_e^2-\omega_{ce}^2\right)\bar{\omega}_e-\hat{\omega}_e^2k^2v_{th,e}^2+\omega_{ce}^2k_z^2v_{th,e}^2},\tag{6}$$

where we have introduced the plasma frequencies defined as $\omega_{pe,i}=\sqrt{n_{e,i}q^2/\varepsilon_0m_{e,i}}$ and χ_i and χ_e are the ion and electron susceptibilities, respectively.

The ionic part of the fluid dispersion in Eq. 6 is similar to the ionic dispersion in Ref.[31], that indeed was retrieved by a fluid ionic model. The only differences are related to the assumption

(cold ions, collisionless plasma, no ion drift) made by Ducrocq *et al.* in their model. The main discrepancies come out in the electron part, where the kinetic DR shows k-resonances that are not captured by the fluid DR. The above 3D dispersion relation cannot be solved analytically to find $\omega = \omega(\mathbf{k})$. However, it can be simplified to retrieve the DRs of interesting waves/instabilities, such as the aforementioned Ion Acoustic Wave[25,26,28], the Modified Two-Stream Instability[27,37,39] and the Ion Transit Time Instability[42,43].

A. Ion Acoustic Wave

1. *The fluid IAW dispersion relation*

The IAW, originally discussed by Gary and Sanderson in Ref.[29], has been observed in both axial-azimuthal and radial-azimuthal 2D PIC simulations[7,17,25,33,39,46,51]. In these works, in particular in Refs.[25,33,39,46], the IAW has been interpreted as the evolution of the ECDI in the saturated regime. In the next section, we propose a kinetic/fluid comparison that clarifies the relation between these two instabilities from a theoretical point of view. In Paper I, we have shown that although the IAW is mainly an azimuthal instability, it has a small axial component (along y). For this reason, in order to obtain the IAW dispersion relation from the general dispersion relation of Eq. (6), we project in the xy-plane while imposing $k_z = 0$. The electron susceptibility then reads

$$\chi_e = -\frac{\omega_{pe}^2}{(\hat{\omega}_e^2 - \omega_{ce}^2)\,\bar{\omega}_e/\hat{\omega}_e - k^2 v_{th,e}^2} = -\frac{1}{k^2\lambda_D^2}\frac{1}{\frac{(\hat{\omega}_e^2-\omega_{ce}^2)\bar{\omega}_e}{\hat{\omega}_e k^2 v_{th,e}^2} - 1}, \tag{7}$$

where the electron Debye length is defined as $\lambda_D^2 = v_{th,e}^2/\omega_{pe}^2$ and $k = \sqrt{k_x^2 + k_y^2}$. This expression can be simplified considering the typical characteristics of the IAW: a wavenumber in the range $\omega_{ce}/v_{th,e} \ll k \ll \omega_{ce}/v_{e,0}$ and a frequency ω in the MHz range (note that $v_{e,0}/\omega_{ce}$ is the distance traveled by the electron guiding center during one period of gyration and $v_{th,e}/\omega_{ce}$ is the gyroradius, hence the condition above implies that $v_{e,0} \ll v_{th,e}$). In this limit, we have $\omega_{ce} \gg \hat{\omega}_e$ and considering a weak collisionality implies that $\bar{\omega}_e \sim \hat{\omega}_e$. From these observations it follows that $\frac{(\hat{\omega}_e^2-\omega_{ce}^2)\bar{\omega}_e}{\hat{\omega}_e k^2 v_{th,e}^2} \ll 1$, which allows to write a rather simple expression for the electron susceptibility, i.e., $\chi_e = 1/k^2\lambda_D^2$. By neglecting ion collisions and ion thermal velocity, we can write an explicit expression for the DR, as

$$\omega_{1,2} = \mathbf{k}\cdot\mathbf{v}_{i,0} \pm \frac{k\lambda_D\omega_{pi}}{(1+k^2\lambda_D^2)^{1/2}}, \tag{8}$$

which is the expression previously proposed by Gary[28]. The DR has no imaginary part and therefore does not predict the growth of an instability. Lafleur *et al.*[23] found from the kinetic theory the same expression for the real part of the DR, accompanied by the following growth rate

$$\gamma_{1,2} \approx \pm\sqrt{\frac{\pi m_e}{8m_i}}\frac{\mathbf{k}\cdot\mathbf{v}_{e,0}}{\left(1+k^2\lambda_D^2\right)^{3/2}}. \tag{9}$$

2. *Comparison with kinetic theory*

The kinetic DR calculated by Krall *et al.*[52–54], considering cold ions and a drifting Maxwellian for electrons, in $k \sim k_y$ limit reads

$$0 = k_y^2\lambda_D^2\left(1-\frac{\omega_{pi}^2}{\omega^2}\right) + \left[1 - I_0(\psi^2)e^{-\psi^2} + \sum_{n=1}^{\infty}\frac{2(\omega-k_y v_{e,0,y})^2 I_n(\psi^2)e^{-\psi^2}}{(n\omega_{ce})^2-(\omega-k_y v_{e,0,y})^2}\right], \tag{10}$$

where $\psi^2 = k_y^2 v_{th,e}^2/\omega_{ce}^2$ and I_n is the modified Bessel function of order n. A complete study of the kinetic DR can be found in the works of Ducrocq *et al.*[31] and Cavalier *et al.*[32]. It is interesting to note that this kinetic DR contains cyclotron resonances, that are not present in the fluid DR calculated in the previous section. These resonances ($k_y \approx n\omega_{ce}/v_{e,0}$) are the well known ECDI modes[23,32].

As noted by Krall[52], the electron cyclotron resonances are related to the angular non-uniformity of the distribution function perturbation. This fact is clearly in contradiction with the hypothesis of a scalar isotropic pressure. The first resonance is simply related to the Lorentz force, i.e., an anisotropy related to the fluid velocity, so it can be predicted by a simplified fluid model.

The comparison of the kinetic DR in Eq. (10) and the fluid one of Eq. (6) in different intervals of k brings some useful insights. If we consider a long wavelength instability such that $k_y \ll \omega_{ce}/v_{th,e}$ (i.e. $k_y^2 v_{th,e}^2 \ll \omega_{ce}^2$, so $\psi^2 \to 0$), we can simplify the kinetic DR considering the terms up to ψ^2. The only Bessel functions contributing to the DR are the ones with $n = 0, 1$. Hence, the simplified kinetic DR reads

$$0 = 1 - \frac{\omega_{pi}^2}{\omega^2} - \frac{1}{k_y^2\lambda_D^2}\frac{k_y^2 v_{th,e}^2}{(\omega-k_y v_{e,0,y})^2-\omega_{ce}^2} \tag{11}$$

and corresponds exactly to the fluid one projected along the $y-$axis (using the electron susceptibility in Eq. (7)) in the collisionless cold plasma limit (i.e. $\hat{\omega}_e = \bar{\omega}_e$ and $v_{th,e,i} \sim 0$). We note that this expression, derived by the fluid theory, predicts the presence of the first cyclotron resonance. However, if we consider the limit in which we have obtained this expression ($k_y \ll$

$\omega_{ce}/v_{th,e}$) and that $v_{e,0,y} < v_{th,e}$, which is true in most of the cases, we observe that the resonance at $k_y = \omega_{ce}/v_{e,0,y}$ disappears, since $k_y v_{e,0,y} < k_y v_{th,e} \ll \omega_{ce}$. In these conditions, the electron susceptibility becomes $\chi_e = \omega_{pe}^2/\omega_{ce}^2$, since $k^2 v_{th,e}^2 \ll |(\omega - k_y v_{e,0,y})^2 - \omega_{ce}^2| \approx \omega_{ce}^2$ and the DR simplifies to $\omega^2 \approx \omega_{ce}^2 \omega_{pi}^2/\omega_{pe}^2$. If we consider a wavenumber as in the previous section (i.e. $\omega_{ce}/v_{th,e} \ll k_y \ll \omega_{ce}/v_{e,0,y}$) we have $e^{-\psi^2} \to 0$ and the kinetic DR in Eq. (10) simplifies to

$$0 = k_y^2 \lambda_D^2 \left(1 - \frac{\omega_{pi}^2}{\omega^2}\right) + 1,$$

that is exactly the fluid expression in Eq. (8) with no ion drift. The limit for $k_y \gg \omega_{ce} v_{e,0,y}$ is easily computed for both fluid and kinetic theories and reads $\omega^2 = \omega_{pi}^2$.

In conclusion, we have shown that in the fluid DR the cyclotron resonances with $n > 1$ are not captured. This can be explained by the fact that the fluid theory is not able to capture the angular asymmetries in the velocity space as the pressure is assumed to be isotropic. In addition, we have shown that in the limit of short and long wavelengths, the kinetic DR simplifies to the fluid DR.

B. Modified Two-Stream Instability

The Modified Two-Stream Instability is a radial-azimuthal instability, proposed by McBride *et al.*[27], that was recently studied in detail by Janhunen *et al.*[37] and Petronio *et al.*[39]. Limiting our interest to the yz-plane, the DR reads

$$0 = 1 - \frac{\omega_{pi}^2}{\omega^2} - \frac{\omega_{pe}^2}{\hat{\omega}_e^2 \dfrac{\hat{\omega}_e^2 - \omega_{ce}^2}{\hat{\omega}_e^2 - k_z^2/k^2 \omega_{ce}^2} - v_{th,e}^2},$$

where we considered a collisionless approximation, (i.e. $\hat{\omega}_e = \bar{\omega}_e = \omega - \mathbf{k} \cdot v_{e,0}$) and no-drifting cold ions (i.e. $v_{i,0} = v_{th,i} = 0$). In the case of cold electrons ($v_{th,e} = 0$), the electron contribution to the DR, χ_e, simplifies to

$$\chi_e = -\frac{k_z^2}{k^2} \frac{\omega_{pe}^2}{(\omega - k_y v_{e,0})^2} - \frac{k_y^2}{k^2} \frac{\omega_{pe}^2 \omega_{ce}^2}{\left((\omega - k_y v_{e,0})^2 - \omega_{ce}^2\right)}.$$

Injecting this expression in the full fluid DR, we obtain

$$0 = 1 - \frac{\omega_{pi}^2}{\omega^2} - \frac{\omega_{pe}^2 k_z^2}{(\omega - k_y v_0)^2 k^2} - \frac{\omega_{pe}^2 k_y^2}{\left((\omega - k_y v_{e,0})^2 - \omega_{ce}^2\right) k^2}. \tag{12}$$

This expression is exactly the one found by Janhunen *et al.*[37] in the case of cold electrons with kinetic theory. In Ref.[39] a complete study of this instability in this limit has been carried out.

C. Ion Transit Time Instability

Hagelaar *et al.*[41], Barral *et al.*[42] and Fernandez *et al.*[43] introduced an axial electrostatic long-wavelength ($\sim 1\,$cm) mid-frequency ($\sim 400\,$kHz) instability that was called Ion Transit-Time Instability (ITTI). This instability is a resistive instability, whose azimuthal propagation was studied by Litvak and Fisch[44]. It is interesting to note that Chable and coworkers[55] studied a similar resistive instability in a low frequency (i.e. below 100 kHz) regime.

As done previously in the IAW, we consider that the wave has both axial and azimuthal components (i.e. $\mathbf{k} = (k_x, k_y, 0)$ with $k_y \ll k_x$). If we neglect the ion thermal velocity $v_{th,i} = 0$ and the effect of electron gyration around magnetic field lines, the DR reads

$$0 = 1 - \frac{\omega_{pi}^2}{\hat{\omega}_i \bar{\omega}_i} - \frac{\omega_{pe}^2}{\hat{\omega}_e \bar{\omega}_e - k^2 v_{th,e}^2}. \tag{13}$$

The ITTI is a rather low-frequency instability, so we have $\omega \ll \omega_{pi}$, and the previous expression simplifies to

$$\frac{\omega_{pi}^2}{\hat{\omega}_i \bar{\omega}_i} = -\frac{\omega_{pe}^2}{\hat{\omega}_e \bar{\omega}_e - k^2 v_{th,e}^2}.$$

Moreover, since the ITTI is mainly axial and the ion drift in azimuthal direction is very small (the ions are not magnetized in these conditions), we have $\mathbf{k} \cdot \mathbf{v}_{i,0} \sim k_x v_{i,0,x}$. As a result, these simplifications yield the following DR

$$\omega_{1,2} = k_x v_{i,0,x} - \frac{m_e}{m_i}\left(\mathbf{k}\cdot\mathbf{v}_{e,0} - \imath\nu_e/2\right) \pm \left(\frac{m_e}{m_i}\left(2\left(\mathbf{k}\cdot\mathbf{v}_{e,0}\right)k_x v_{i,0,x} - \left(\mathbf{k}\cdot v_{e,0}\right)^2 + k^2 v_{th,e}^2\right) - \left(\frac{m_e}{m_i}\frac{\nu_e}{2}\right)^2 + \imath\nu_e\frac{m_e}{m_i}\left(\mathbf{k}\cdot\mathbf{v}_{e,0} - k_x v_{i,0,x}\right)\right)^{1/2}. \tag{14}$$

Fernandez *et al.*[43] used a model similar to the one proposed here for the ions, while they considered a drift/diffusion model for electrons, obtaining eventually a 1D-version of the DR in Eq. (14). By neglecting electron gyration we are reducing our model to drift/diffusion as well. Note that this result corresponds to a situation of quasi-neutrality for the plasma. Recently, Koshkarov *et al.*[45] demonstrated that the effect of the finite Larmor radius and the electron inertia must be taken into account to have an instability growth rate vanishing at infinity. The effect of instability-driven turbulence in 2D is investigated in Koshkarov *et al.*[56].

Limit behavior of the ITTI

We define the two branches in Eq. (14) *plus* and *minus* waves (identified by the sign prior to the square root) and we designate them with the subscripts p and m, respectively. We observe that each branch can be stable or unstable (i.e. have a positive or negative imaginary part), depending on the plasma parameters and an easy simplification of the radicand in the ITTI DR can explain why. We observe that the real part of this radicand is largely dominated by the *thermal* term (i.e. $k^2 v_{th,e}^2 \gg 2\,(\mathbf{k}\cdot\mathbf{v}_{e,0})\,k_x v_{i,0,x} - (\mathbf{k}\cdot v_{e,0})^2$) and, considering some reasonable values for the wavenumber, we also have that $m_e/m_i k^2 v_{th,e}^2 \gg \nu_e \frac{m_e}{m_i}(\mathbf{k}\cdot\mathbf{v}_{e,0} - k_x v_{i,0,x})$. Then, after some algebraic manipulation, real and imaginary parts of the simplified DR can be rewritten

$$\begin{aligned} \omega_{p,m} &= k_x(v_{i,0,x} \pm c_s), \\ \gamma_{p,m} &= \frac{\nu_e}{2}\frac{m_e}{m_i}\frac{kc_s \pm (k_y v_{e,0,y} - k_x v_{i,0,x})}{kc_s}, \end{aligned} \tag{15}$$

where $c_s = \sqrt{m_e/m_i}\,v_{th,e}$. In these equations we observe that the real part does not depend on the azimuthal direction, while the imaginary part does: the growth rate in Eq. (15) is proportional to the azimuthal electron drift (term $\nu_e \frac{m_e}{m_i} k_y v_{e,0,y}$). One may notice in Eq. (15), that the growth rate does not vanish for large k. As mentioned earlier, Koshkarov *et al.*[45] demonstrated that considering a finite Larmor radius and electron inertia results in a stabilization of the large wavenumbers. Eq. (15) can also be used to derive a stability condition for the *plus* and *minus* waves: *plus* wave is unstable if

$$v_{i,0,x} < c_s + v_{e,0,y}k_y/k_x$$

and the *minus* wave is unstable if

$$v_{i,0,x} > -c_s + v_{e,0,y}k_y/k_x.$$

The ITTI is usually present downstream of the ion sonic point[46], where $v_{i,0,x} > c_s$, so if we consider a purely axial propagation ($k_y = 0$), the stability conditions presented above only allow the growth of the *minus* wave, as it was observed by Fernandez *et al.*[43]. The growth of the *plus* wave is only allowed downstream (i.e. where $v_{i,0,x} > c_s$), if we consider a non-null azimuthal component of the wavevector. This underlines the importance of considering both directions: the driver of the ITTI instability is a combination of the electron azimuthal motion with the ionic axial motion.

III. THE AXIAL-AZIMUTHAL INSTABILITIES IN PIC

In Paper I we discussed the development of plasma electrostatic instabilities in Hall Thruster PIC/MCC simulations and we have shown how these instabilities can be detected by the PSD2P. In these simulations the neutral gas dynamics is solved with an HLLC scheme and the discharge is coupled with an *RLC* circuit. The ionization is self-consistently calculated within the MCC module: this allows the growth and development of the breathing mode. In this section, we study the main characteristics of the IAW and the ITTI instabilities and we compare the spectrum calculated from PIC data to the one predicted by the analytic development of Section II. The test case analyzed in the present Section is a $4\,\mathrm{cm} \times 4\,\mathrm{cm}$ simulation with a low electron temperature of injection at the cathode (i.e. $T_e^{cath} = 0.1\,\mathrm{eV}$), in which the instabilities can be easily distinguished: the IAW is stronger during the growing phase of the breathing mode, while the ITTI is dominating when the current decreases.

A. The IAW in two dimensions

The Ion Acoustic Wave has been studied as a purely azimuthal instability in several works[25,35,39,46,57], while, in Paper I, we observed that this instability has an axial signature as well. In Section II A we derived a bi-dimensional dispersion relation (see Eq. (7)) for the IAW. By extracting λ_D, ω_{pi} and $\mathbf{v}_{i,0}$ from PIC data and substituting these values in Eq. (8), we can obtain the IAW frequency for different values of k_x and k_y. Figure 1 (a) shows a map of the IAW frequency for values of k_x and k_y in a typical range for IAW.

Since we are assuming that $k_x \neq 0$ and $k_y \neq 0$, the comparison of this DR map with a simulation spectrum requires a 3D transform of a signal in the $x-y-t$ space, which is not achievable in a convenient way. This issue can be overcome by considering that the main component of the IAW is an ECDI-like almost-purely azimuthal oscillation (i.e. such that $k_y \gg k_x$), represented as the black arrow in Figure 1 (a), with an azimuthal wavenumber $k_y^{\max}$. Thus, we can assume that the IAW is an instability developing around the $(k_x \approx 0, k_y \approx k_y^{\max})$ point in the $k-$space. When we perform a spectral analysis in the azimuthal direction, we then have to compare it with the 1D analytic DR calculated along the blue line in Figure 1(a), which corresponds to a dispersion $\omega_{1,2}^{\mathrm{azimuth}}(k_y) = \omega_{1,2}(k_y, k_x \sim 0)$ that is equivalent to the one commonly calculated for the 1D IAW. Oppositely, the 1D axial DR must be calculated considering that the azimuthal wavenumber component is not

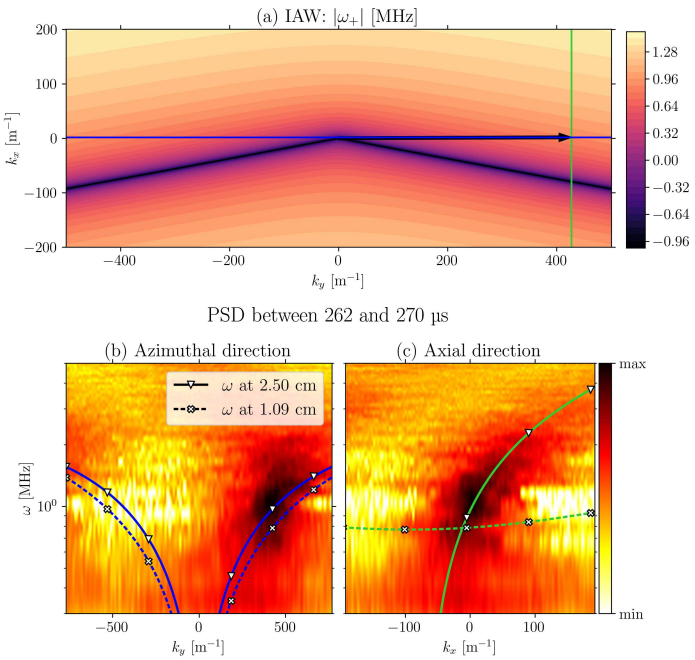

FIG. 1: (a) Numerical solution of Eq. (8) with plasma parameters extracted from PIC simulations (4 cm × 4 cm axial-azimuthal domain with an electron temperature of injection at the cathode of 0.1 eV) at the axial position of $x = 2.5$ cm, corresponding to the channel exit. Bottom: Azimuthal (b) and Axial (c) PSD2P map calculated at the channel exit. The green and blue lines in (b) and (c) represent the azimuthal and axial projections of the IAW as shown in (a). The dashed lines in (b) and (c) show the DR calculated inside the channel, while the solid lines represent the DR calculated at the channel exit.

negligible and has a constant value $k_y^{\max}$. Thus, the dispersion that we observe in the axial direction corresponds to the one calculated along the green line in Figure 1 (a), i.e. $\omega_{1,2}^{\text{axial}}(k_x) = \omega_{1,2}(k_y \approx k_y^{\max}, k_x)$. The coefficients of these equations are calculated by averaging over y and over time the plasma parameters extracted from the PIC simulation. The value of $k_y^{\max}$ is calculated from the PSD2P numerical spectrum in the azimuthal direction.

A representation of these DRs is given in Figures 1 (b) and (c), where the blue and green lines represent the 1D DRs calculated along the corresponding lines in Fig. 1 (a). The two color-plots in these figures, displaying the azimuthal and axial PSD2Ps, are discussed and compared to the analytic DRs in subsection III A 2. Here, we only emphasize the significant effect of the choice of the axial position at which we extract the plasma parameters: the axial DR varies drastically from the thruster inner channel to the channel exit.

1. Temporal evolution of the IAW amplitude

In order to study the evolution of the IAW during a BM cycle, we take six time intervals of 8 µs, spanning from the start to the end of a BM cycle, as shown in Figure 2(a). For each time interval, we perform an axial and an azimuthal PSD2P at several positions along the thruster axis and we calculate from these PSD2P maps the intensity of the IAW peak (by summing axial and azimuthal contributions). Figure 2(b) confirms that the IAW intensity profiles change significantly during the breathing mode, as it was observed in Paper I. The study of the evolution of these profiles gives important insights about the growth and development of the ion acoustic instability.

At the beginning of the growing phase of the BM (Fig. 2(c)), we observe that the IAW develops mainly in the external part of the channel and in the plume (blue line in Figure 2(b)), with a maximum at $x \sim 1.75$ cm, while almost no IAW is detected in the thruster inner channel. This observation remains true in the BM growing phase (green, orange and yellow lines, i.e., Figs. 2(d, e, f)), where we observe that the maximal IAW intensity stays between $x = 1.5$ and 2 cm, and progresses slightly towards the anode at each the subsequent time interval. The IAW amplitude in the plume is smaller than the maximum and approximately constant in space, increasing at each timestep of the growing BM phase. In the channel region near the anode, almost no IAW is detected in the first two intervals (blue and green). At t =254 µs we observe a consistent growth of the IAW also in this region, even if the IAW intensity near the anode remains significantly lower than the one at the thruster exit.

In the decreasing phase of the BM (magenta and brown lines, i.e., Figs. 2(g, h)) we observe a major change in the IAW characteristics. The instability starts to move towards the anode, while in the central part of the thruster almost no IAW is detected and a weaker residual IAW is detected in the plume region. The absolute value of the maximum, that is now near the anode, decreases. This means that a part of the instability energy has been dissipated or convected out of the simulation

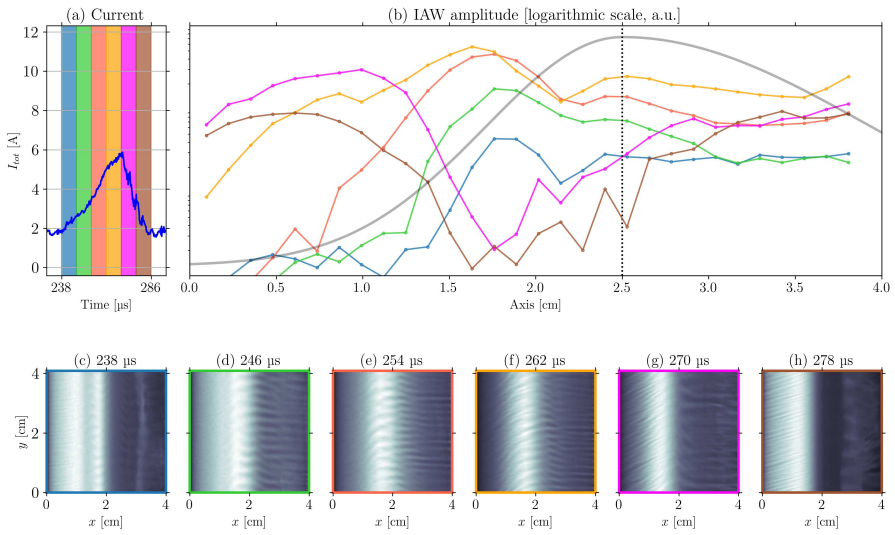

FIG. 2: (a) The discharge current evolution during a given BM oscillation. The different color bands indicate the six time-intervals where we performed the PSD2P. In (b) we show the amplitude of the IAW mode along the thruster axis, each color line corresponds to the time interval with the same color in (a). The solid black line and the vertical dashed black line represent the magnetic field shape and its maximum axial position, respectively. In (c-h) we show 6 snapshots of the plasma density n_e at the beginning of each of the six time-intervals.

domain at the anode boundary. Similarly, the wave amplitude in the plume decreases: this is consistent with the observations of Paper I where the IAW almost disappears in the plume during the BM decreasing phase, that is dominated by the ITTI.

The analysis of the evolution of the IAW amplitude performed in this section using the PSD2P technique suggests that: (1) the instability forms at the beginning of the BM growing phase at a position near the channel exit, (2) during the whole BM growing phase the instability strengthens at the channel exit and in the plume and starts to propagate also in the region next to the anode, (3) eventually, in the BM decreasing phase, the IAW loses most of its energy at the cathode exit and in the plume, where the ITTI becomes dominant (i.e. see paper I), while it remains prevailing near the anode, even if it loses some of its energy.

2. *The origin of the IAW*

Although the discussion in the previous section has already given some important insights about the origin of the IAW instability, the comparison of the PSD2P maps with the analytic DR improves significantly our understanding of the growth of this instability. Since the shape of the spectrum along the thruster axis for $x > 2\,\mathrm{cm}$ is rather constant and, as we see in Figure 2(b), the amplitude does not vary either, we chose to calculate the PSD2Ps at the channel exit ($x = 2.5\,\mathrm{cm}$, see Figure 1(b) and (c)), and then to compare them to the analytic results obtained by Eq. (8). Obviously, since we want to study how the analytic DR varies when we change the time and the axial position, we work in a bi-dimensional parametric-space, that is difficult to compare to the dispersion relations maps obtained with the PSD2P. In order to identify the right time and axial position at which the instability forms, we dynamically adjusted the time and position of the calculation, verifying that the best fit of the PSD2P maps is obtained calculating the dispersion at the beginning of the growing phase of the Breathing Mode, which is consistent with what we observed in the previous section. Similarly, we calculated the IAW analytic axial and azimuthal DRs at several axial positions, comparing them to the PSD2P maps. An example is shown in Figure 1 (b) and (c), where we plotted two DRs: one calculated in the channel near the anode (dashed line) and the other at the thruster exit (solid line). In Fig. 1 (b) we can see that both the dispersion calculated in the channel and the dispersion calculated in the plume fit the azimuthal spectrum calculated with the PSD2P. Hence, it is difficult to conclude anything about the instability origin using only the spectrum in azimuthal direction. As we have seen, the spectrum in axial direction, reported in Fig. 1(c), has a well-defined shape, that helps us to identify the position where likely the IAW forms. We observe that the axial dispersion $\omega_{1,2}^{\mathrm{axial}}(k_x)$ calculated at the channel exit is consistent with the spectrum, while the one calculated using the parameters extracted in the channel near the anode is not. Thus, these observations suggest that the instability is not originated from the channel and then convected outwards, as proposed in Ref.[46], but rather that the IAW arises in the central part of the simulation (between the density peak and the max of the magnetic field). This view is consistent with what has been observed in section III A 1 concerning the evolution of the instability intensity.

The previous observation about the position at which the IAW originates can be consolidated by studying the characteristics of the IAW growth rate, calculated using kinetic theory by Lafleur *et al.*[24], the result of which is given in Eq. (9). In Figure 3(a) we observe that in azimuthal direction

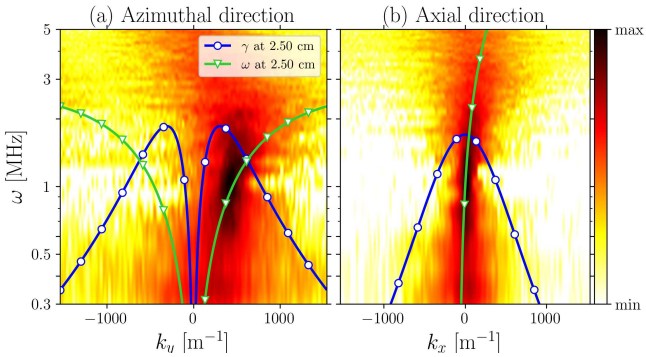

FIG. 3: In (a) and (b) the 2D color plots show the PSD in azimuthal and axial directions, respectively. In green we draw the best IAW DR as in Figure 1. The corresponding growth rate (magnified by a factor 8) is plotted in blue.

the maximal growing wavenumbers are rather well predicted by the analytic γ, as already noticed in several other works[25,39,46]. The novelty is given by the result in (b), where we observe that the expression in Eq. (9) predicts the growth of a low-k_x mode, as it is actually observed. From Eq. (9) one can easily compute the maximal value of the growth rate in the case of a purely azimuthal instability, as

$$\gamma_{max} \approx \gamma\left(k_y = \frac{1}{\sqrt{2}\lambda_D}, k_x \approx 0\right) = \sqrt{\frac{\pi m_e}{54 m_i}}\frac{v_{e,0,y}}{\lambda_D}, \tag{16}$$

which is proportional to the ratio between the azimuthal drift of electrons and the Debye length. The axial profiles of these quantities at the beginning of the BM cycle are shown in Figure 4(a) and the corresponding maximal growth rate profile is shown in Figure 4(b). Observation of this profile shows a weak growth rate in the channel near the anode and in the plume. Definite evidence of a significant growth rate is observed in the central part of the simulation, with a plateau between ~ 1.4 and 2.7 cm. This corroborates the idea that the instability primarily grows in the external part of the discharge channel and subsequently propagates towards the anode and the cathode. In Figure 5 we observe that the ion flow is subsonic in the anode region (i.e. $x \lesssim 1.7$ cm), which allows the propagation of the plasma wave. On the contrary, when the flow becomes strongly supersonic in the plume region we expect that a phenomenon of instability convection will couple with the propagation of the wave.[25] In Figure 5 we report a schematic of propagation and wave convection.

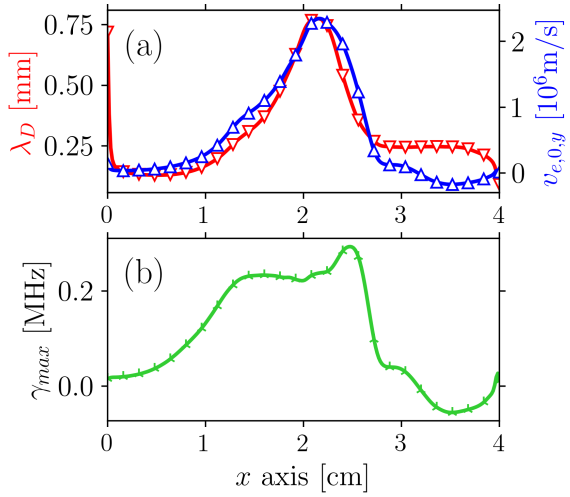

FIG. 4: (a) Debye length (red) and electron azimuthal drift velocity (blue) mean profiles between 234 and 238 s. (b) Maximum growth rate from Eq.(16). We remind the reader that the value of λ_D has been increased by a factor 8 by scaling the permittivity.

3. *The cause of the bending of the IAW instability*

Several works[16,22,47,58] have reported the fact that the IAW/ECDI instability is purely azimuthal in the plume, while it propagates with a non-zero k_x component in the region next to the anode. In order to understand the reason why we observe a change in the instability direction we propose an analogy with the classical Snell theory of sound waves propagation in media with different sound velocity[59]. This theory (that can be extended from perfect gases to plasmas without further approximations) suggests that the propagation velocity of sound waves depends on the gas temperature.

As already discussed in Paper I, the PSD2P technique successfully captures the bending of the wavefronts, thus it can be used to study the evolution of the instability along the thruster axis. We have calculated the PSD reconstructed spectrum in axial and azimuthal directions at four different axial positions and the corresponding 8 PSD2P maps are shown in Figure 6. In this figure, the subfigures (a-d) display the axial PSD at different axial positions and the subfigures (f-i) show the corresponding azimuthal ones. In (e) we show a snapshot taken at $t = 263\,\mu$s of the electron

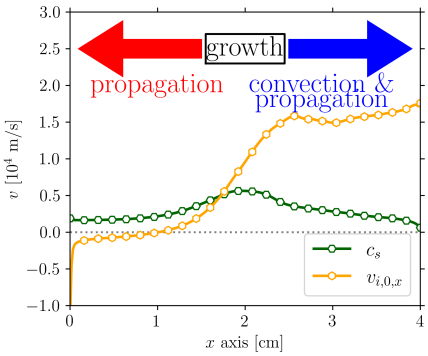

FIG. 5: The axial profiles of sound speed and ion axial velocity calculated at $t = 262\,\mu$s. The arrows indicate the direction of propagation and convection of the wave.

density and, superimposed to it, we draw the four arrows indicating the instability propagation direction determined by the main components calculated in the PSD2P spectra. The instability propagates with $k_x \neq 0$ in the channel near the anode, as one can notice in Figs 6 (a) and (f), then the wavefronts fold in a position near the electron temperature peak and the instability direction becomes parallel to the azimuthal direction. Observing the subfigure pairs (c,h) and (d,i) we notice that the spectral maps do not vary much in the plume, and that the axial and azimuthal dispersion relations of IAW (calculated as in the previous sections) successfully fit the dispersion maps at both positions.

The propagation without energy losses of a plane wave at an interface of two media implies the conservation of the wave frequency, otherwise the wave energy is not conserved. So, just considering that the parallel (to the interface of two media) wavenumber is conserved and that the wave velocity varies at the interface, we can easily obtain the Snell law for plane waves as

$$\text{cotan}\theta \mathrm{d}\theta = \frac{\mathrm{d}v}{v},$$

where θ is the propagation angle with respect to the normal to the interface and $v = \omega/k$ is the wave speed. Considering two regions of thickness δx, as shown in Figure 7, we can write the Snell law as

$$\frac{\sin\theta_1}{v_1} = \frac{\sin\theta_2}{v_2}, \tag{17}$$

where $v_{1,2}$ are the phase velocities in the two zones and $\theta_{1,2}$ are the corresponding angles. Ex-

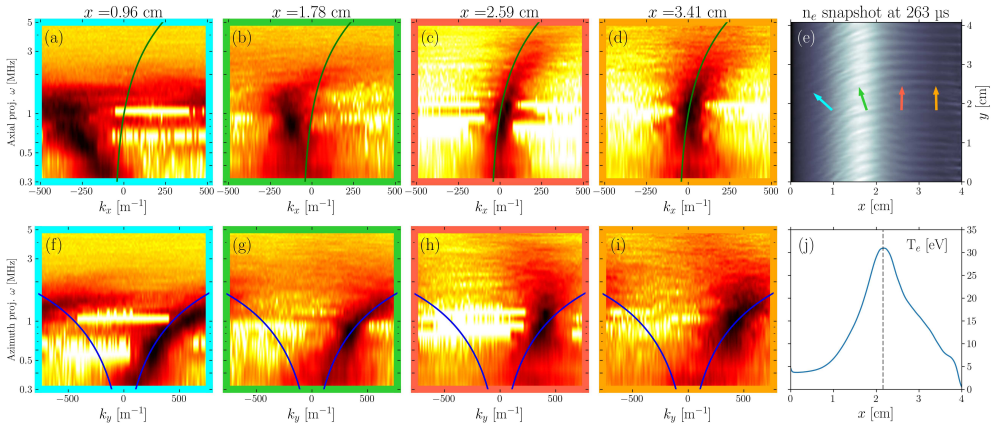

FIG. 6: (a-d) PSD2P calculated in the axial direction at four different axial positions indicated above each figure. The green lines represent the axial IAW calculated as in Fig. 1. (f-i) PSD2P calculated in the azimuthal direction at the same axial positions. The blue lines represent the azimuthal IAW calculated as in Fig. 1. In (e) a snapshot of the electron density map at $t = 263\,\mu s$ is shown. The arrows represent the instability direction, that is calculated by the k_x and k_y in the spectra. Each frame corresponds to the arrow with the same color. In (j) we show the electron temperature axial profile at $t = 263\,\mu s$.

tending the classical gas theory to plasma, at first approximation we assume that the hotter is the plasma, the higher is the propagation velocity of IAW. This is consistent with the result in Eq. 8, that suggest that this oscillation propagates at the Bohm speed, that is proportional to $T_e^{1/2}$. So, considering an instability forming in the region between the temperature peak and the thruster exit in the first phase of the BM growing phase, its propagation towards the anode is blocked by the temperature peak, that behaves as a barrier. By considering two propagation velocities v_1 and v_2, such that $v_1 < v_2$, corresponding to a lower temperature and an higher temperature, respectively, we use the Snell law to clearly explain the nature of this phenomenon. Using such velocities in Eq. 17, we have that the refraction angle θ_2 of a wave propagating almost parallel to the azimuthal direction ($\sin\theta_1 \sim 1$) is such that

$$\sin\theta_2 = \frac{v_2}{v_1} > 1.$$

Hence, this relation suggests that the propagation is forbidden from a zone with lower temperature

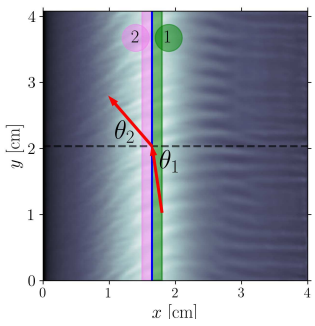

FIG. 7: Schematic of the Snell refraction of an instability propagating from the region 1 of thickness δx with propagation velocity v_1 to the region 2 where the propagation velocity is $v_2 < v_1$.

to a zone with higher temperature and successfully explains the *barrier* behavior of the temperature peak. Moreover, this theory is confirmed by the slow instability convection towards the temperature peak that we observe in Figure 2(b). The situation is different when we consider the region between the maximal temperature position and the anode. In this zone the electron temperature decreases (from right to left), so does the propagation velocity, and the wave propagation towards the anode is not anymore forbidden. The Snell-behavior hypothesis proposed in this section can be quantitatively validated by comparing along the $x-$axis the propagation angle of the main IAW mode (corresponding to the PSD2P intensity peak) calculated directly in the PSD2P maps with one estimated by Snell wave propagation formula.

Using axial and azimuthal PSD2P maps and selecting the values corresponding to the PSD peak we identified the values of $\omega_{\max}$, $k_{x,\max}$ and $k_{y,\max}$, corresponding to the intensity peak. In Figure 8(a) we observe that the direction of the vector identified by the pair ($k_{x,\max}$, $k_{y,\max}$) successfully represent the wavefront propagation direction. The propagation angle measured with respect to the x axis, as θ_2 in Figure 7, is estimated by calculating the arctangent of $k_{y,\max}/k_{x,\max}$ and is plotted in Figure 8(b) using blue markers. In order to apply the Snell method just described, we need to know the main mode phase velocity. It can be estimated by the ratio between the frequency $\omega_{\max}$ and wavenumber $k_{\max}$, this last obtained as $k_{\max} = \sqrt{k_{x,\max}^2 + k_{y,\max}^2}$. The considerations made in the previous sections suggest that the propagation starts at the axial position x_1 at the right of the temperature peak ($x_1 = 2.25\,\mathrm{cm}$). Thus, taking the velocity v_1 and angle θ_1

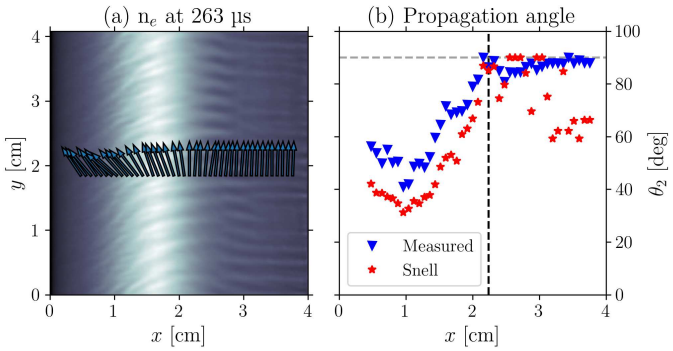

FIG. 8: (a) An electron density snapshot and (b) the angle measured by PIC simulations (blue dots) and the one calculated using the Snell law (red dots).

at this position, from the velocity v_2 at a generic position x_2 we can calculate using Eq. 17 the corresponding propagation angle θ_2. Using this method, we estimate the propagation angle at every axial position, obtaining the angles represented by the red marks in Figure 8(b). The comparison of the angles directly measured in the simulation with the ones estimated by the Snell law shows a good agreement all along the thruster axis, confirming the validity of our model. However, Figure 8 requires some additional discussion: firstly, we hypothesize that the origin of the underestimation of the angle in the channel is due to the fact that we analyze a single time interval and we do not consider the complex evolution of the propagation reported in previous sections. Secondly, we think that the badly estimated angles in the plume are related to the rather spread out PSD2P spectra measured in this region, as visible by Figure 6(i). Moreover, a phenomenon of instability convection may be present in this region of the simulation[25].

The model presented here helps us to interpret the IAW amplitude variation in Figure 2(b). The IAW cannot propagate from a colder to an hotter region, since a hotter plasma corresponds to a larger propagation velocity. Thus, the IAW instability that develops in the central part of the simulation domain, is slowly convected towards the temperature peak and only a tiny fraction of its intensity can actually pass the barrier. When most of the instability power reaches the temperature peak and the temperature starts to decrease (at the beginning of the BM decreasing phase), the propagation is not anymore forbidden, so the instability propagates in the colder plasma at a different angle. In the previous discussion we assumed a rather simple relation of proportionality of the IAW propagation speed with the plasma temperature, that is probably true at first approxi-

mation, but that should be analyzed more in detail, since other factors may also play a role in this relation.

B. The Ion Transit-Time Instability

As shown in Paper I, the ITTI develops in the external part of the channel and in the plume, mainly in the decreasing BM phase. In this Section, we study the analytic DR derived in Section II and we compare it to PSD2P maps that were obtained from PIC data, demonstrating the importance of considering the 2D nature of the ITTI.

1. The ITTI 2D spectrum

As mentioned in Paper I, the ITTI is difficult to capture since it mainly develops along the thruster axis and the standard techniques (i.e., based on the FFT) do not allow for studying the spectrum along this direction. Fernandez *et al.*[43] have calculated an ITTI 1D dispersion relation by using fluid equations (continuity and momentum for ions, while the electrons are described by the continuity equation and by a drift-diffusion equation in which they introduced a collision frequency depending on the anomalous electron mobility). In Section II C, we have shown that an equivalent DR with two branches (Eq. (14)) can be obtained just by considering continuity and momentum equation for both electrons and ions. In addition, Fernandez *et al.* observed that the dispersion map calculated from their numerical experiment at the thruster exit was better described by the *plus* instability branch, with reference to the branches nomenclature given in section II C. However, they found the paradox that in the 1D approximation this branch is stable. Here we have shown that for $k_y \neq 0$ the *plus* branch has a positive growth rate and can be unstable.

Most of the parameters that appear in the ITTI DR can be estimated directly from the PIC simulation, while for the collision frequency appearing in Eq. (15) it is more subtle, because the fluid model does not take into account the well-known anomalous mobility. If we consider the classical collision frequency measured in the simulation we obtain growth rates in the kHz range, very far from what we observe in the PIC simulations. However, as suggested by Fernandez *et al.*, we can consider an *anomalous* collisionality depending on the anomalous mobility. The anomalous electron mobility in axial direction (i.e. $\mu_{e,x}$) can be expressed, including the electron

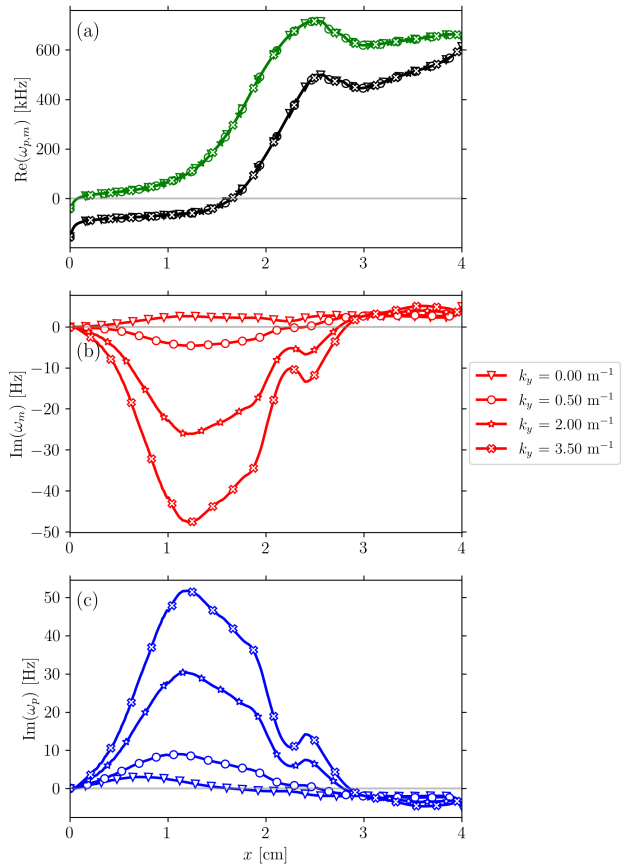

FIG. 9: (a) The axial profile of the two ITTI branches for $k_x = 40\,\mathrm{m}^{-1}$. The *plus* branch is traced in green and the *minus* branch in black. In (b) and (c) the lines represent the profile of γ_m (red) and γ_p (blue) for four different values of k_y.

pressure gradient, by the PIC results as

$$\mu_{e,x} = \frac{v_{e,x}}{E_x + \nabla(n_e k_b T_e)/n_e e}$$

and the collision frequency can then be estimated by the usual mobility formula for magnetized plasmas: $\nu_e = m_e \omega_{ce}^2 \mu_{e,x}/e$. Once we have calculated the anomalous frequency, we only need to

properly choose the values of axial and azimuthal wavenumbers to plot the ITTI growth rate profile along the x-axis. In Paper I we observe that the ITTI axial wavenumber can be estimated from the PSD2P maps and takes a value of $k_x \approx 40\,\mathrm{m}^{-1}$, while the azimuthal wavenumber is more difficult to estimate because of the rather broad azimuthal PSD. For this reason, in Figure 9 we calculate using the full ITTI dispersion (i.e. Eq. (14)) the axial profile of $\omega_{p,m}$ and $\gamma_{p,m}$ for four different values of k_y, always considering $k_x = 40\,\mathrm{m}^{-1}$. To have a better estimation of the growth-rate it is necessary to consider the finite electron Larmor radius and electron inertia terms[45]. Figure 9(a) confirms the weak dependence of the real part of the dispersion on the value of k_y, as predicted by the simplified DR in Eq. (15). On the contrary, the imaginary part of the dispersion strongly depends on the value of k_y. If k_y is strictly equal to zero, we observe that the *minus* wave is unstable all along the axis, while the *plus* wave is unstable in the channel and damped in the plume. We observe that the *minus* wave is more damped for increasing values of k_y while the *plus* wave becomes increasingly unstable. In particular, we observe that the most unstable point of the profile is close to the ion sonic point, that was identified as the point where the ITTI grew[46].

In Figure 10, we show the numerical PSD2P calculated during a BM decreasing phase in the thruster plume. We observe that the ITTI *plus* wave calculated by Eq. (14) at the ion sonic point describes perfectly the dispersion from PIC simulations, while the *minus* wave corresponds to lower frequencies. This result, compared with the analysis in Figure 9, strengthens the idea that we need to consider an azimuthal component of the ITTI to predict the growth of the branch that is actually observed. As reported in Paper I, the main instability frequency calculated by the PSD2P is $\omega_{ITTI} \sim 350\,\mathrm{kHz}$ and propagates with a wavenumber $k_{ITTI} \sim 40\,\mathrm{m}^{-1}$ in the axial direction. In Figure 10(a) we do not plot the azimuthal DR since the ITTI dispersion relation has been calculated in the small-k_y limit and it would be appropriate to plot it only for $k_y \ll k_x^{\max}$.

We can conclude that the ITTI, as the IAW, has a preferential direction (i.e. axial in this case), but that we need to consider a 2D dispersion relation to properly describe the instability growth. In particular, we have shown that the electron azimuthal drift is a paramount component of the ITTI growth rate.

2. *The effect of the ITTI on the discharge current*

In this section, we study the effect of the ITTI on a macroscopic parameter, the discharge current, that is usually analyzed in experiments through discrete Fourier transform (DFT) techniques[60].

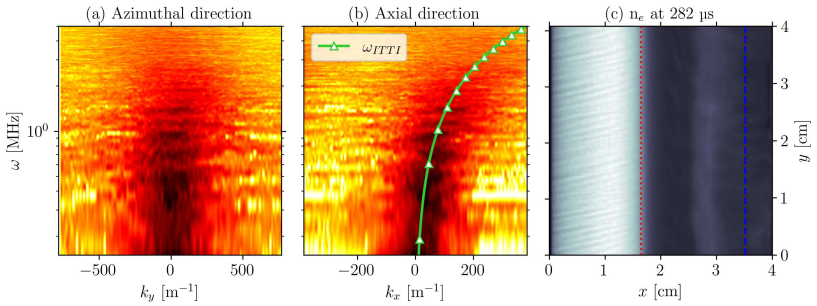

FIG. 10: Azimuthal (a) and axial (b) PSD2Ps. In (c) a snapshot of the electron density at $t = 282\,\mu s$ is shown. The green line in (b) represents the ITTI frequency, calculated as in Eq. (14). The vertical dotted red line in (c) reports the position of the ion sonic point and the vertical dash-dotted blue line represents the axial position at which the PSD2P is calculated. The dispersion in azimuthal direction is not displayed, since the expression in Eq. (14) was calculated in the small k_y limit.

The discharge current that is measured in the PIC simulations at quasi-steady state is shown in Figure 11(a). In this figure, we can distinguish six BM periods. As reported in Paper I and in previous sections, the ITTI is stronger during the BM decreasing phase. For this reason, we expect that the effect of the ITTI on the discharge current will be visible mainly during this phase. In Fig. 11(b) we zoom on a single BM period and we clearly observe a modulation of the discharge current in the BM decreasing phase, that is not present in the BM growing phase. The large BM fluctuations in this simulation make extremely difficult to observe precisely the ITTI in performing an FFT on the entire discharge current (even after a high-pass filtering of the current signal). To overcome this issue, we have calculated the five spectra in the six BM decreasing phases, where the ITTI oscillation is stronger, obtaining the results in Figure 11(c). The average spectrum in Figure 11(d) evokes the presence of a modulation of the current at $\approx$300 kHz, that is exactly corresponding to the ITTI main frequency found in Paper I.

The ITTI is an ion instability, but until now the origin of this name could be unclear. In the previous paragraph we have shown that it is possible to link the discharge current to the ITTI oscillations, but the mechanism has not been discussed yet. To illustrate it, in Figure 12 we study a single ITTI period (the one between the two vertical black lines in Fig. 12 (a)). Looking at the evolution of the axial ion density profile in Figure 12(b), we notice that the ITTI has a weak

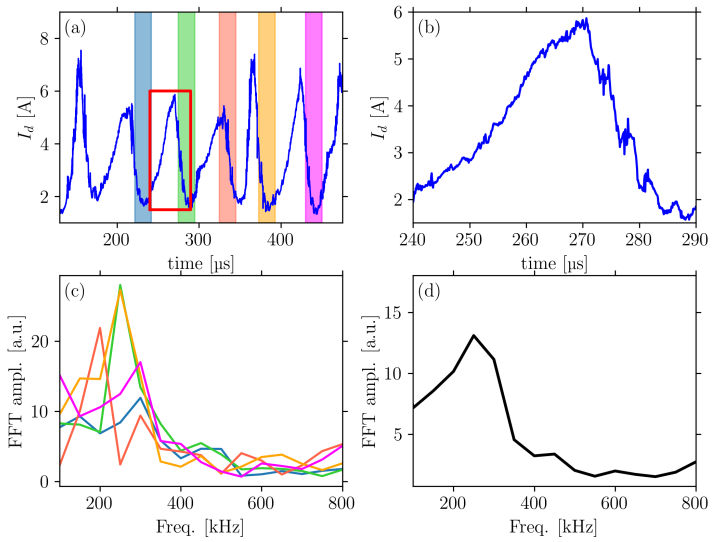

FIG. 11: (a) the discharge current during several periods of the BM. (b) a zoom of the discharge current between 275 and 295 µs. (c) FTTs calculated from the current with the same color in (a). (d) the average spectrum.

impact on the density in the channel region, while the transit of ions is clearly visible in the acceleration region. Between $t = 276.9\,\mu s$ and $279.3\,\mu s$ we observe a packet of ions moving along the acceleration region towards the cathode, actually creating the current modulation that we have observed. Interestingly, as soon as the packet has reached the cathode another packet starts to form at the beginning of the acceleration region. This behavior can be understood looking at the axial electric field shape in (c). We notice an electric field well moving as the ions packet. This is particularly visible at $t = 279.66\,\mu s$, when the formation of the new packet of ions is sustained by the creation of a well in the electric field profile.

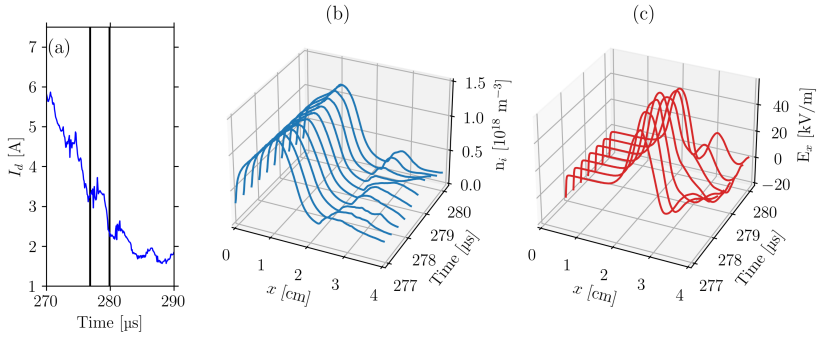

FIG. 12: (a) The discharge current in a decreasing phase of the BM. The two vertical black lines bound a single ITTI oscillation. For this ITTI oscillation, in (b) and (c), we show the time evolution of the ion density and of the axial electric field, respectively.

IV. CONCLUSION

In this work, we have derived an expression for the 3D dispersion relation (DR) of electrostatic instabilities in $\mathbf{E}\times\mathbf{B}$ discharges, starting from a standard fluid model (continuity and momentum equation for electrons and ions) that considers Poisson equation. We have shown that it is possible to extract from it some simplified DRs that correspond to the most common instabilities observed in $\mathbf{E}\times\mathbf{B}$ discharges, in particular the Ion Acoustic Wave (IAW) and the Ion Transit-Time Instability (ITTI) developing in the axial-azimuthal (xy) plane of Hall thrusters. This work shows that all electrostatic instabilities usually observed in HT can be derived by the same 3D DR by projecting in different planes and considering the right wavenumbers.

In Hall Thrusters, the IAW is usually considered as a purely azimuthal instability. In the present work, we have shown that it is important to consider the bi-dimensional nature of this instability to understand its growth and evolution. The two-point power spectral density reconstruction technique (PSD2P) allowed us to demonstrate the good agreement between the spectral maps calculated in axial and azimuthal directions with the analytic DR. Moreover, the analysis of a sequence of time intervals has shown that this instability develops at the external part of the thruster channel (i.e. near the channel exit between 2 and 2.5 cm in this paper case) and subsequently propagates inwards (towards the anode) and outwards (towards the cathode). Calculating the spectrum at different axial positions with the PSD2P technique has allowed to study the shape of this instability

along the thruster axis. With a simple analogy with the propagation of acoustic waves in media with different refractive indexes we have explained how the temperature gradient in the inner part of the thruster channel generates the change of direction of the propagation fronts.

The ITTI is usually considered as a purely axial instability. In this work, we have calculated the ITTI dispersion relation with a non-zero azimuthal component. The $k_y \neq 0$ has a weak impact on the real part of the DR, that is well described by a purely axial DR. However, it has a strong effect on the imaginary part of the DR and it explains why the *plus* wave is observed, and not the *minus* wave. When we considered an anomalous collisionality (related to the anomalous mobility in the axial direction), the ITTI growth rate is consistent with the growth time that we observe in the PIC simulations. It is possible to identify the packets of ions traveling from the density peak outwards (the ITTI is an instability related to the ion transit in acceleration region) and to recognize their effect on the discharge current. This observation suggests a possible way to detect experimentally this instability on real devices.

ACKNOWLEDGMENTS

FP acknowledges financial support from a Safran Aircraft Engines doctoral research award as well as from the Association Nationale de la Recherche et de la Technologie (ANRT) as part of a CIFRE convention. This work has been partially funded by ANR (n^o ANR-16-CHIN-003-01) and Safran Aircraft Engines with the project POSEIDON. This work was granted access to the HPC resources of CINES under the allocations A0100510439 and A0120510439 made by GENCI.

DATA AVAILABILITY

The data that support the findings of this study are available from the corresponding author upon reasonable request.

REFERENCES

[1]A. I. Morozov and V. V. Savelyev, FUNDAMENTALS OF STATIONARY PLASMA THRUSTER THEORY (Springer, 2000).

[2]D. M. Goebel and I. Katz, Fundamentals of Electric Propulsion: Ion and Hall Thrusters, JPL SPACE SCIENCE AND TECHNOLOGY SERIES (Wiley, 2008).

[3]M. J. Rycroft and N. Crosby, Smaller Satellites: Bigger Business?: Concepts, Applications and Markets for Micro/Nan Vol. 6 (Springer Science & Business Media, 2013).

[4]J. Vaudolon, V. Vial, N. Cornu, and I. Habbassi, "PPSRX00 Thruster Development Status at Safran," (36th International Electric Propulsion Conference - Vienna, 2019).

[5]K. Hara, "An overview of discharge plasma modeling for Hall effect thrusters," Plasma Sources Science and Technology **28**, 044001 (2019).

[6]F. Taccogna and L. Garrigues, "Latest progress in Hall thrusters plasma modelling," Reviews of Modern Plasma Physics **3**, 12 (2019).

[7]J.-P. Boeuf, "Tutorial: Physics and modeling of Hall thrusters," Journal of Applied Physics **121**, 011101 (2017).

[8]I. D. Kaganovich, A. Smolyakov, Y. Raitses, E. Ahedo, I. G. Mikellides, B. Jorns, F. Taccogna, R. Gueroult, S. Tsikata, A. Bourdon, J.-P. Boeuf, M. Keidar, A. T. Powis, M. Merino, M. Cappelli, K. Hara, J. A. Carlsson, N. J. Fisch, P. Chabert, I. Schweigert, T. Lafleur, K. Matyash, A. V. Khrabrov, R. W. Boswell, and A. Fruchtman, "Physics of E B discharges relevant to plasma propulsion and similar technologies," Physics of Plasmas **27**, 120601 (2020).

[9]A. I. Smolyakov, O. Chapurin, W. Frias, O. Koshkarov, I. Romadanov, T. Tang, M. Umansky, Y. Raitses, I. D. Kaganovich, and V. P. Lakhin, "Fluid theory and simulations of instabilities, turbulent transport and coherent structures in partially-magnetized plasmas of $\mathbf{E}\times\mathbf{B}$ discharges," Plasma Physics and Controlled Fusion **59**, 014041 (2017).

[10]T. Andreussi, V. Giannetti, A. Leporini, M. M. Saravia, and M. Andrenucci, "Influence of the magnetic field configuration on the plasma flow in Hall thrusters," Plasma Physics and Controlled Fusion **60**, 014015 (2018).

[11]I. G. Mikellides and I. Katz, "Numerical simulations of Hall-effect plasma accelerators on a magnetic-field-aligned mesh," Physical Review E **86**, 046703 (2012).

[12]J. C. Adam, J. P. Boeuf, N. Dubuit, M. Dudeck, L. Garrigues, D. Gresillon, A. Heron, G. J. M. Hagelaar, V. Kulaev, N. Lemoine, S. Mazouffre, J. Perez Luna, V. Pisarev, and S. Tsikata,

"Physics, simulation and diagnostics of Hall effect thrusters," Plasma Physics and Controlled Fusion **50**, 124041 (2008).

[13]J. Bak, R. Kawashima, G. Romanelli, and K. Komurasaki, "Plasma structure and electron cross-field transport induced by azimuthal manipulation of the radial magnetic field in a Hall thruster E B discharge," Journal of Applied Physics **131**, 053302 (2022).

[14]A. L. Raisanen, K. Hara, and I. D. Boyd, "Two-dimensional hybrid-direct kinetic simulation of a Hall thruster discharge plasma," Physics of Plasmas **26**, 123515 (2019).

[15]T. Lafleur, R. Martorelli, P. Chabert, and A. Bourdon, "Anomalous electron transport in Hall-effect thrusters: Comparison between quasi-linear kinetic theory and particle-in-cell simulations," Physics of Plasmas **25**, 061202 (2018).

[16]T. Charoy, J. P. Boeuf, A. Bourdon, J. A. Carlsson, P. Chabert, B. Cuenot, D. Eremin, L. Garrigues, K. Hara, I. D. Kaganovich, A. T. Powis, A. Smolyakov, D. Sydorenko, A. Tavant, O. Vermorel, and W. Villafana, "2D axial-azimuthal particle-in-cell benchmark for low-temperature partially magnetized plasmas," Plasma Sources Science and Technology **28**, 105010 (2019).

[17]W. Villafana, F. Petronio, A. C. Denig, M. J. Jimenez, D. Eremin, L. Garrigues, F. Taccogna, A. Alvarez Laguna, J. P. Boeuf, A. Bourdon, P. Chabert, T. Charoy, B. Cuenot, K. Hara, F. Pechereau, A. Smolyakov, D. Sydorenko, A. Tavant, and O. Vermorel, "2D radial-azimuthal particle-in-cell benchmark for E B discharges," Plasma Sources Science and Technology **30**, 075002 (2021).

[18]J. M. Fife, Hybrid-PIC Modeling and Electrostatic Probe Survey of Hall Thrusters, Ph.D. thesis, Massachusetts Institute of Technology (1999).

[19]J. J. Szabo, Fully kinetic modeling of a plasma thruster, Ph.D. thesis, Massachusetts Institute of Technology (2001).

[20]E. Ahedo, J. M. Gallardo, and M. Martínez-Sánchez, "Effects of the radial plasma-wall interaction on the Hall thruster discharge," Physics of Plasmas **10**, 3397–3409 (2003).

[21]J. C. Adam, A. Héron, and G. Laval, "Study of stationary plasma thrusters using two-dimensional fully kinetic simulations," Phys. Plasmas **11**, 12 (2004).

[22]P. Coche and L. Garrigues, "A two-dimensional (azimuthal-axial) particle-in-cell model of a Hall thruster," Physics of Plasmas **21**, 023503 (2014).

[23]T. Lafleur, S. D. Baalrud, and P. Chabert, "Theory for the anomalous electron transport in Hall effect thrusters. II. Kinetic model," Physics of Plasmas **23**, 053503 (2016).

[24]T. Lafleur, S. D. Baalrud, and P. Chabert, "Theory for the anomalous electron transport in Hall effect thrusters. I. Insights from particle-in-cell simulations," Physics of Plasmas **23**, 053502 (2016).

[25]T. Lafleur and P. Chabert, "The role of instability-enhanced friction on 'anomalous' electron and ion transport in Hall-effect thrusters," Plasma Sources Science and Technology **27**, 015003 (2017).

[26]T. Lafleur, S. D. Baalrud, and P. Chabert, "Characteristics and transport effects of the electron drift instability in Hall-effect thrusters," Plasma Sources Science and Technology **26**, 024008 (2017).

[27]J. B. McBride, "Theory and Simulation of Turbulent Heating by the Modified Two-Stream Instability," Physics of Fluids **15**, 2367 (1972).

[28]S. P. Gary, "Longitudinal waves in a perpendicular collisionless plasma shock: II. Vlasov ions," Journal of Plasma Physics **4**, 753–760 (1970).

[29]S. P. Gary and J. J. Sanderson, "Longitudinal waves in a perpendicular collisionless plasma shock: I. Cold ions," Journal of Plasma Physics **4**, 739–751 (1970).

[30]C. Lashmore-Davies and T. Martin, "Electrostatic instabilities driven by an electric current perpendicular to a magnetic field," Nuclear Fusion **13**, 193–203 (1973).

[31]A. Ducrocq, J. C. Adam, A. Héron, and G. Laval, "High-frequency electron drift instability in the cross-field configuration of Hall thrusters," Physics of Plasmas **13**, 102111 (2006).

[32]J. Cavalier, N. Lemoine, G. Bonhomme, S. Tsikata, C. Honoré, and D. Grésillon, "Hall thruster plasma fluctuations identified as the EB electron drift instability: Modeling and fitting on experimental data," Physics of Plasmas **20**, 082107 (2013).

[33]T. Charoy, T. Lafleur, A. Tavant, P. Chabert, and A. Bourdon, "A comparison between kinetic theory and particle-in-cell simulations of anomalous electron transport in E B plasma discharges," Physics of Plasmas **27**, 063510 (2020).

[34]S. Tsikata and T. Minea, "Modulated Electron Cyclotron Drift Instability in a High-Power Pulsed Magnetron Discharge," Physical Review Letters **114**, 185001 (2015).

[35]Z. A. Brown and B. A. Jorns, "Spatial evolution of small wavelength fluctuations in a Hall Thruster," Physics of Plasmas **26**, 113504 (2019).

[36]A. Héron and J. C. Adam, "Anomalous conductivity in Hall thrusters: Effects of the nonlinear coupling of the electron-cyclotron drift instability with secondary electron emission of the walls," Physics of Plasmas **20**, 082313 (2013).

[37]S. Janhunen, A. Smolyakov, D. Sydorenko, M. Jimenez, I. Kaganovich, and Y. Raitses, "Evolution of the electron cyclotron drift instability in two-dimensions," Physics of Plasmas **25**, 082308 (2018).

[38]L. Wang, A. Hakim, B. Srinivasan, and J. Juno, "Electron cyclotron drift instability and anomalous transport: two-fluid moment theory and modeling," arXiv:2107.09874 [physics] (2021), arXiv: 2107.09874.

[39]F. Petronio, A. Tavant, T. Charoy, A. Alvarez Laguna, A. Bourdon, and P. Chabert, "Conditions of appearance and dynamics of the modified two-stream instability in E B discharges," Physics of Plasmas **28**, 043504 (2021).

[40]I. G. Mikellides and A. L. Ortega, "Growth of the modified two-stream instability in the plume of a magnetically shielded Hall thruster," Physics of Plasmas **27**, 100701 (2020).

[41]G. Hagelaar, J. Bareilles, L. Garrigues, and J.-P. Boeuf, "Role of anomalous electron transport in a stationary plasma thruster simulation," Journal of Applied Physics **93**, 67–75 (2003).

[42]S. Barral, K. Makowski, Z. Peradzyński, and M. Dudeck, "Transit-time instability in Hall thrusters," Physics of Plasmas **12**, 073504 (2005).

[43]E. Fernandez, M. K. Scharfe, C. A. Thomas, N. Gascon, and M. A. Cappelli, "Growth of resistive instabilities in EB plasma discharge simulations," Physics of Plasmas **15**, 012102 (2008).

[44]A. A. Litvak and N. J. Fisch, "Resistive instabilities in hall current plasma discharge," Physics of Plasmas **8**, 648–651 (2001).

[45]O. Koshkarov, A. I. Smolyakov, I. V. Romadanov, O. Chapurin, M. V. Umansky, Y. Raitses, and I. D. Kaganovich, "Current flow instability and nonlinear structures in dissipative two-fluid plasmas," Physics of Plasmas **25**, 011604 (2018).

[46]T. Charoy, T. Lafleur, A. Alvarez Laguna, A. Bourdon, and P. Chabert, "The interaction between ion transit-time and electron drift instabilities and their effect on anomalous electron transport in Hall thrusters," Plasma Sources Science and Technology **30**, 065017 (2021).

[47]K. Hara and S. Tsikata, "Cross-field electron diffusion due to the coupling of drift-driven microinstabilities," Physical Review E **102**, 023202 (2020).

[48]P. Kumar, S. Tsikata, and K. Hara, "Effects of multiply charged ions on microturbulence-driven electron transport in partially magnetized plasmas," Journal of Applied Physics **130**, 173307 (2021).

[49]T. Lafleur, P. Chabert, and A. Bourdon, "The origin of the breathing mode in Hall thrusters and its stabilization," Journal of Applied Physics **130**, 053305 (2021).

[50]O. Chapurin, A. I. Smolyakov, G. Hagelaar, and Y. Raitses, "On the mechanism of ionization oscillations in Hall thrusters," Journal of Applied Physics **129**, 233307 (2021).

[51]V. Croes, T. Lafleur, Z. Bonaventura, A. Bourdon, and P. Chabert, "2D particle-in-cell simulations of the electron drift instability and associated anomalous electron transport in Hall-effect thrusters," Plasma Sources Science and Technology **26**, 034001 (2017).

[52]N. A. Krall and M. N. Rosenbluth, "Trapping Instabilities in a Slightly Inhomogeneous Plasma," Physics of Fluids **5**, 1435 (1962).

[53]N. A. Krall and M. N. Rosenbluth, "Low-Frequency Stability of Nonuniform Plasmas," Physics of Fluids **6**, 254 (1963).

[54]N. A. Krall and D. L. Book, "Ion Sound Instability in a Collisionless Shock Wave," Physics of Fluids **12**, 347 (1969).

[55]S. Chable and F. Rogier, "Numerical investigation and modeling of stationary plasma thruster low frequency oscillations," Physics of Plasmas **12**, 033504 (2005).

[56]O. Koshkarov, A. Smolyakov, Y. Raitses, and I. Kaganovich, "Self-Organization, Structures, and Anomalous Transport in Turbulent Partially Magnetized Plasmas with Crossed Electric and Magnetic Fields," Physical Review Letters **122**, 185001 (2019).

[57]Z. Asadi, F. Taccogna, and M. Sharifian, "Numerical Study of Electron Cyclotron Drift Instability: Application to Hall Thruster," Frontiers in Physics **7**, 140 (2019).

[58]T. Ben Slimane, C. Honoré, T. Charoy, A. Bourdon, and P. Chabert, "Analysis of small scale fluctuations in Hall effect thrusters using virtual Thomson scattering on PIC simulations," Physics of Plasmas **29**, 023501 (2022).

[59]A. D. Pierce, Acoustics: An Introduction to Its Physical Principles and Applications (Springer International Publishing, Cham, 2019).

[60]E. T. Dale and B. A. Jorns, "Experimental characterization of Hall thruster breathing mode dynamics," Journal of Applied Physics **130**, 133302 (2021).

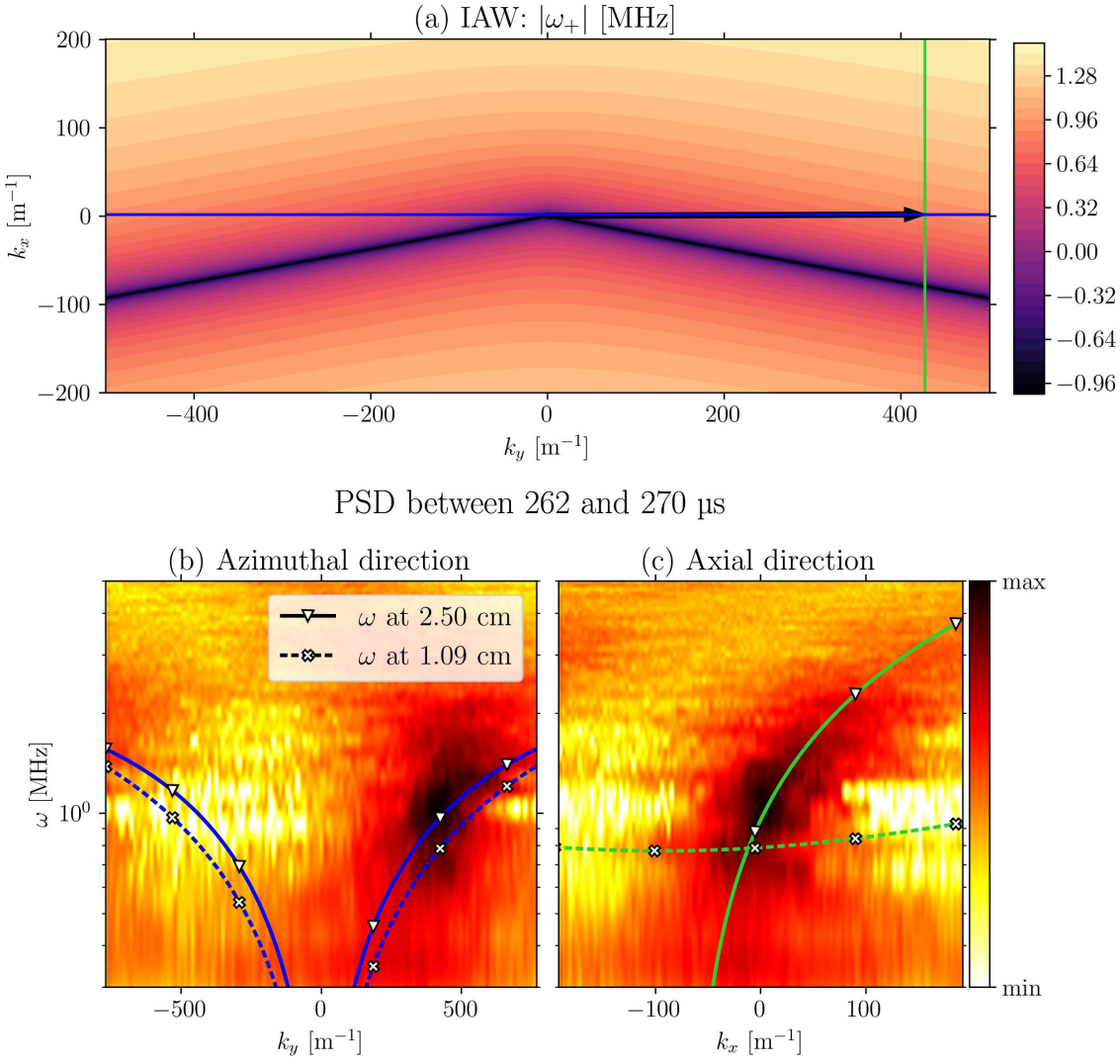

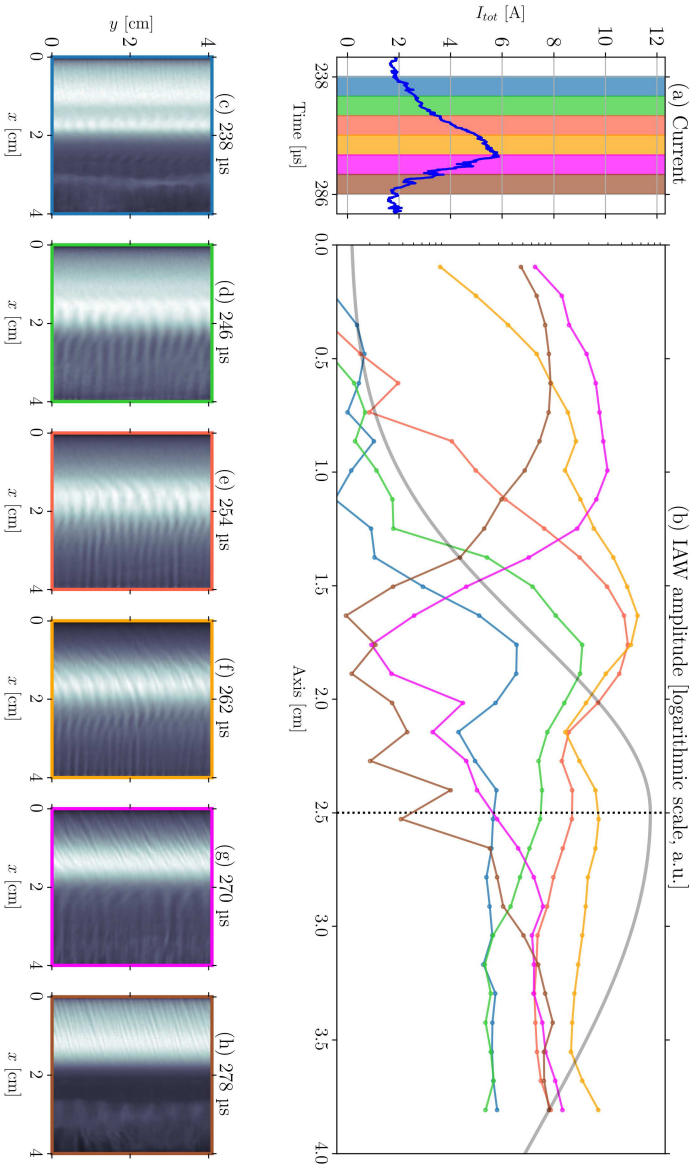

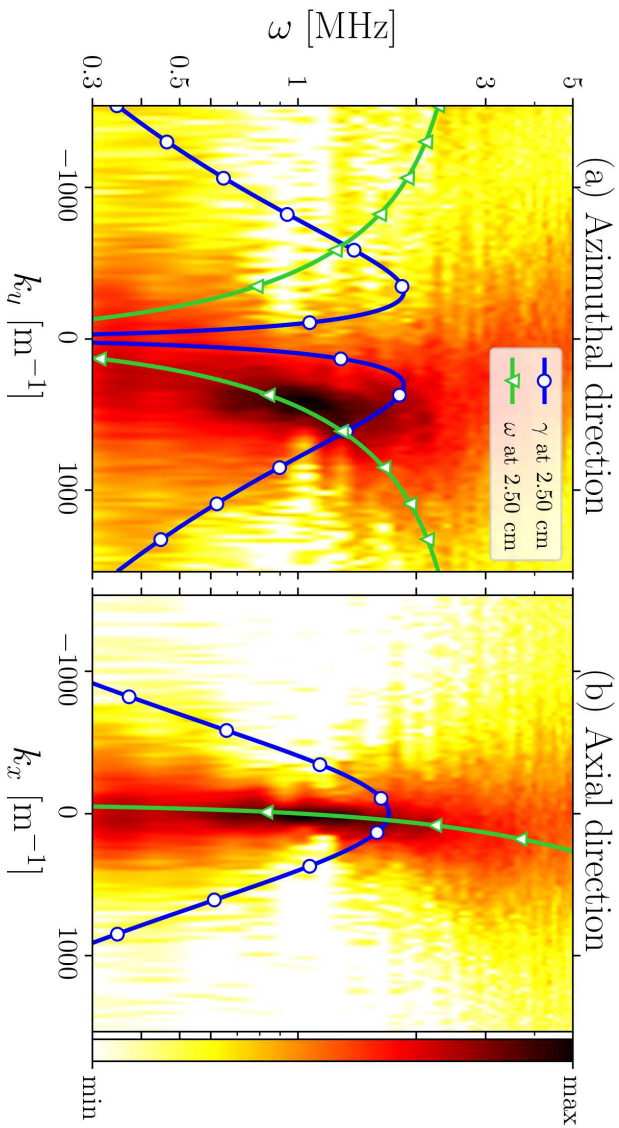

PLEASE CITE THIS ARTICLE AS DOI: 10.1063/5.0119255